

Towards a monotonicity-preserving inviscid wall boundary condition for aeroacoustics

I. Spisso * and A. Rona †

Department of Engineering, University of Leicester, Leicester, LE1 7RH, UK

E. H. Georgoulis ‡

Department of Mathematics, University of Leicester, LE1 7HR, UK

Abstract

This paper presents an extension of the Tam and Dong solid wall boundary condition that combines the established non-penetration physical condition with a further restriction on the wall-normal velocity gradient. This results in a wall boundary condition in the form of a second-order partial differential equation which is satisfied analytically by fully reflecting acoustic waves and is monotonicity preserving in problems with a dominant near-boundary acoustic pressure distribution. With the extended wall boundary condition discretized to second-order spatial accuracy, tests on the wall reflection of a two-dimensional Gaussian pulse show that this condition suppresses the high wavenumber spurious numerical waves from the more conventional $v = 0$ formulation. This result is obtained using a compact finite-difference time-marching scheme that is sixth-order accurate in space and fourth-order accurate in time without the use of high-order filters applied to the computational domain interior.

I. Introduction

Defining accurate and stable non-reflecting boundary conditions is one of the most challenging aspects in the development of Computational Aeroacoustic codes (CAA).¹⁻³ The CAA algorithms used in aeroacoustics are required to resolve high frequency short waves with the minimum number of mesh points per wavelength and to minimize the numerical dispersion and dissipation associated to long-distance wave propagation. High-order schemes are able to meet these requirements thanks to their spectral-like resolution properties.⁴ High-order methods are combined with appropriate non-reflecting boundary conditions at the computational boundaries to preserve the interior scheme properties on approach to the boundaries.^{1,5,6}

On a computational domain discretized in space by a characteristic mesh size Δx , physical waves of non-dimensional wavenumber $k\Delta x < \pi$ can be represented without aliasing. Past studies^{5,7} have shown that, when a high-order finite-difference scheme is used to model the reflection of an acoustic wave by a solid wall, the numerical solution contains three distinct components. The first component is the reflected wave, that it is a well-resolved wave, with $k\Delta x \ll \pi$, travelling with a group velocity that closely approximates the local speed of sound c . The second component consists of a spurious poorly resolved wave (grid-to-grid oscillation), with $k\Delta x \approx \pi$, which travels with unphysical group velocity. This wave has been referred in the literature as the *spurious* or *parasite numerical wave* after Vichnevetsky.⁸ As the group velocity of the parasite numerical wave can be much greater than the fastest propagation characteristic of the original hyperbolic (Euler) or parabolic (Navier-Stokes) system of governing equations, it can quickly contaminate the full computational domain. The third component is formed by spatially damped waves, that form a numerical boundary layer in the proximity of a wall surface.⁵

To dampen the parasite numerical waves in the interior of the computational domain, targeted dissipative

*Marie Curie EST Fellow, Department of Engineering, is71@le.ac.uk, AIAA Member

†Lecturer, Department of Engineering, ar45@le.ac.uk, AIAA Member

‡Senior Lecturer, Department of Mathematics, Emmanuil.Georgoulis@mcs.le.ac.uk

techniques are used,⁹ such as explicit artificial selective damping,^{10,11} selective damping by optimized upwind finite difference,¹² and compact filtering.^{4,13,14} Tam and Dong⁵ proposed a technique for the stable discretization of the wall-normal pressure gradient near a solid wall boundary by using one or two ghost points located outside the physical domain. The ghost values are used to calculate the normal gradient of the pressure at the wall, after that all physical quantities, except the ghost values for pressure, are updated at the end of the each time step. To calculate the flow state at the wall, no-slip and isothermal (or adiabatic) conditions, or simply the non-penetration Dirichlet type condition for the inviscid case, are applied.¹³

In this work, the authors apply a new technique where an artificial damping numerical term is added to the classical non-penetration condition for the normal component of velocity at the wall. This way, the gradient is forced to be monotonic in the wall-boundary inwards normal direction for CAA problems with a strong acoustic field. This technique prevents the formation of grid to grid oscillations (*parasite numerical waves*) in the near-wall region.

This paper is organized as follows: Section II introduces the numerical scheme used in the interior of the computational domain, and shows the stability and convergence tests in one and two dimensions. Section III-A recalls the mathematical formulation of the wall boundary conditions for a high-order scheme⁵ and introduces the author’s own wall boundary condition. Section III-B shows a two-dimensional example to demonstrate the effectiveness of the proposed wall boundary condition compared to the classical non-penetration condition.

II. Numerical method

A. Spatial differentiation

1. Finite-difference scheme

Consider a uniformly spaced mesh where the nodes are indexed by i . The discretized spatial coordinates and the scalar flow state at the nodes are respectively given by $x_i = h(i - 1)$ and $f_i = f(x_i)$ for $1 \leq i \leq N$. The finite difference approximation f'_i to the first derivative $(df/dx)(x_i)$ at node i is obtained by solving the tridiagonal system:

$$\alpha f'_{i-1} + f'_i + \alpha f'_{i+1} = b \frac{f_{i+2} - f_{i-2}}{4h} + a \frac{f_{i+1} - f_{i-1}}{2h} \quad (1)$$

where α , a and b determine the dispersion and dissipation properties of the algorithm.⁴ The present authors use the sixth-order prefactored compact version of equation 1 by Hixon, where the non-prefactored operator f' is split in a forward a backward component, so that the stencil on the right-hand side of the equation 1 is reduced from five to three points, with the tridiagonal matrix on the left-hand side replaced by two independent bi-diagonal matrices.^{15,16}

2. Boundary stencils

The numerical performance of the boundary stencil of a compact scheme has a much larger effect on the stability and accuracy of the scheme than the boundary stencil of the equivalent explicit scheme.¹⁷⁻¹⁹ This is because the error from the boundary stencil derivative can propagate well into the computational domain.²⁰ To compute the state variables at the computational domain boundaries and wall points, explicit sixth-order one-sided derivative stencils are defined for the sixth-order compact scheme.¹⁶

In realistic simulations, computational boundaries exist where the flow data are known on both sides of the boundaries (periodic, symmetry, inter-block boundaries), so an appropriate interior differencing scheme at these boundaries has to be used. An explicit central boundary stencil is used for this purpose. This stencil mimics the performance of the compact interior stencil over the resolved range of wavenumbers; it is a 11-point explicit stencil, and it matches the Taylor series of the interior stencil to the ninth order, with the last coefficient used to more closely match the boundary stencil performance with the interior stencil.¹⁶

B. Time integration

To advance a semi-discrete equation in time, the Runge-Kutta time marching method is used. In particular, the classical fourth-order four-stage explicit Runge-Kutta time-marching scheme is employed. The time

evolution equation is re-written as:

$$\frac{\partial}{\partial t} \mathbf{U} = F(\mathbf{U}) \quad (2)$$

where \mathbf{U} represents the vector containing the solution values at spatial mesh point, and the operator $F(\mathbf{U})$ contains the discretization of the spatial derivatives. The fourth-order four-stage Runge-Kutta scheme advances the solution from time level $t = t_n$ to $t_n + \Delta t$ using:

$$\begin{aligned} h^{(p)} &= -\Delta t \frac{d}{dx} \left(F \left(U^n + \alpha_{p-1} h^{(p-1)} \right) \right) \\ U^{n+1} &= U^n + h^{(4)} \end{aligned} \quad (3)$$

for $p = 1, 4$, where α_p are the classical Runge-Kutta coefficients²¹ and $\alpha_0 = 0$.

Using this time marching method, the sixth-order prefactored compact scheme is stable up to a Courant number of 0.49. This scheme is fourth-order accurate in time for linear problems and second-order accurate for non-linear problems. This method has been previously tested and found to be accurate and stable for unsteady problems.²²

C. Numerical stability

1. 1-D scalar equation

To verify the order of accuracy of the method of sections **II-A** and **II-B** and demonstrate the stability characteristics of the periodic boundary closures combined with the interior scheme, consider the one-dimensional scalar advection equation

$$\frac{\partial u}{\partial t} + \frac{\partial u}{\partial x} = 0, \quad 0 \leq x \leq 1, \quad t \geq 0 \quad (4)$$

with the initial condition

$$u(x, 0) = \sin(2\pi x) \quad (5)$$

Equation 4 is solved numerically over the domain $0 \leq x \leq 1$, on a progressively refined uniform mesh. The interior scheme is combined with a cyclic condition at $x = 0$ and $x = 1$ to avoid any possible source of error from the boundary closure. The solutions are integrated over a long time for asymptotic stability. The compact scheme is used to discretize the spatial operators, and the fourth-order, four-stage Runge-Kutta scheme is used to time-march the solution. The Courant number is kept under the stability limit of 0.49. The non-dimensional time step $\Delta \tilde{t}$ and the finite displacement $\Delta \tilde{x}$ in x are selected so that sixth-order accuracy is maintained. Given that the error rate of convergence $\epsilon = (\Delta \tilde{t})^4 + (\Delta \tilde{x})^6$, by imposing $(\Delta \tilde{t}) = (\Delta \tilde{x})^{3/2}$ then sixth-order accuracy is maintained. $(\Delta \tilde{t}) = (\Delta \tilde{x})^{3/2}$ also satisfies the stability constraint

$$CFL = \frac{\Delta \tilde{t}}{\Delta \tilde{x}} = (\Delta \tilde{x})^{1/2} \leq 0.49 \quad (6)$$

Equation 4 has the analytical solution:

$$u_{exact}(x, t) = \sin(2\pi(x - t)) \quad (7)$$

and the L_2 norm of the difference between the analytical and the numerical prediction is calculated as:

$$L_2 = \sqrt{\frac{\sum_{i=1}^N (u_i - u_{exact})^2}{N}} \quad (8)$$

where N is the number of grid points.

Figure 1(a) shows the comparison between the numerical and the analytical solution of the one-dimensional scalar advection equation at time $\tilde{t} = 10$, using a uniform grid spacing equal to $\Delta \tilde{x} = 0.05$. Figure 1(b) shows the L_2 norm for various levels of mesh refinement at the same computational time of $\tilde{t} = 10$. In the loglog plot of figure 1(b), the L_2 norm decreases with a constant slope parallel to the line from a sixth order

exponential. Therefore the scheme maintains sixth-order accuracy with the cyclic boundary condition up to a value of $L_2 \approx 10^{-14}$, close to the machine error. For comparison, the interior scheme coupled with an 11-point explicit stencil boundary condition¹⁴ is also shown in figure 1(b). In this case, the scheme starts to lose its order of accuracy scaling at $L_2 \approx 10^{-8}$, due to the single-precision (7 digits) of the 11-point explicit stencil coefficients.¹⁶

2. Propagation of a 2-D acoustic pulse on unbounded domain

Problem 2 tests the isotropy property of the computational algorithm in two dimensions. It consists of a two-dimensional propagation of an acoustic disturbance superimposed on a uniform mean flow of density ρ_0 , pressure p_0 in a fluid at rest ($u_0 = v_0 = 0$), with no solid boundary.²³ It is required to solve the Linearized Euler Equations (LEE):

$$\frac{\partial \mathbf{U}}{\partial t} + \frac{\partial \mathbf{E}}{\partial x} + \frac{\partial \mathbf{F}}{\partial y} = 0 \quad (9)$$

where the vectors \mathbf{U} , \mathbf{E} , and \mathbf{F} are

$$\mathbf{U} = \begin{bmatrix} \rho \\ u \\ v \\ p \end{bmatrix}, \quad \mathbf{E} = \begin{bmatrix} \rho_0 u \\ p/\rho_0 \\ 0 \\ \gamma p_0 u \end{bmatrix}, \quad \mathbf{F} = \begin{bmatrix} \rho_0 v \\ 0 \\ p/\rho_0 \\ \gamma p_0 v \end{bmatrix} \quad (10)$$

Let the x - y plane be divided into a $N \times N$ Cartesian uniform mesh of spacing Δx and Δy in the x and y directions, with l and m the indices of mesh points, respectively. The computational domain extent is $-50 \leq x \leq 50$, $-50 \leq y \leq 50$. At $t = 0$, the initial flow conditions are:

$$\begin{aligned} p &= p_0 \left[1 + \varepsilon e^{[-(\ln 2) \left(\frac{x^2 + y^2}{9} \right)]} \right] \\ \rho &= \rho_0 \left[1 + \frac{\varepsilon}{\gamma} e^{[-(\ln 2) \left(\frac{x^2 + y^2}{9} \right)]} \right] \\ u &= v = 0 \end{aligned}$$

Non-dimensional values for density $\tilde{\rho}$, pressure \tilde{p} , time \tilde{t} , x -velocity \tilde{u} and v -velocity \tilde{v} are obtained by normalizing with respect to: $l_0 = 0.25 \text{ m}$, $c_0 = 340.29 \text{ m/s}$, and $t_0 = l_0/4c_0$ seconds. At the computational boundaries, explicit sixth-order one-sided boundaries stencils from section II-A-2 are used to preserve the global order of accuracy. The computation is advanced in time up to the non-dimensional time $\tilde{t} = 120$, before the pulse reaches the computational boundaries, to validate the order of accuracy of the numerical scheme.

The results are compared against the non-dimensional analytical perturbation values given in the first workshop on benchmark problems in Computational Aeroacoustics:²³

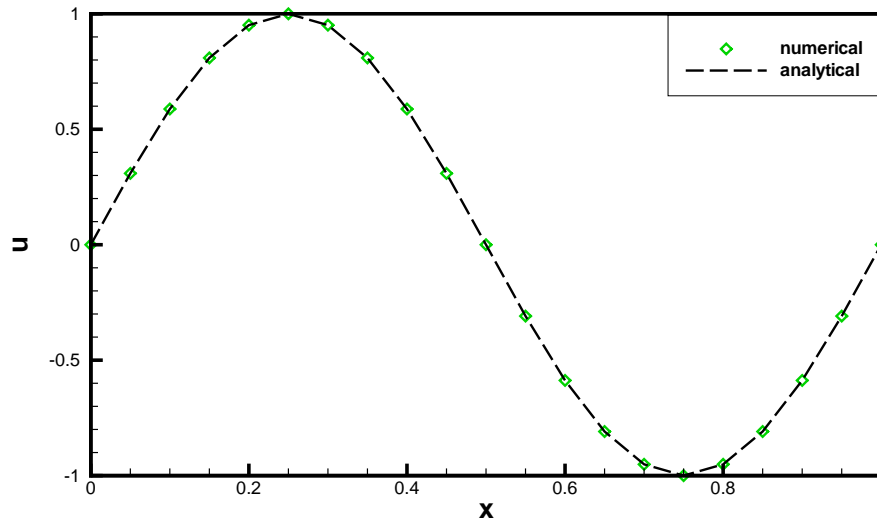
$$\tilde{p}' = \tilde{\rho}' = \frac{1}{2\alpha_1} \int_0^\infty e^{-\xi^2/4\alpha_1} \cos(\xi\tilde{t}) J_0(\xi\eta) \xi d\xi \quad (11)$$

where the superscript ($'$) denotes a perturbation value, $\alpha_1 = [(\ln 2)/9]$, $\eta = [(x^2 + y^2)]^{1/2}$ and $J_0()$ is the zeroth-order Bessel function of the first kind. The evaluation of the integral in eq. 11 has been done numerically with MATLAB®7.3.0 using the adaptive Lobatto quadrature where the absolute error tolerance has been set equal to $1.0e - 12$.

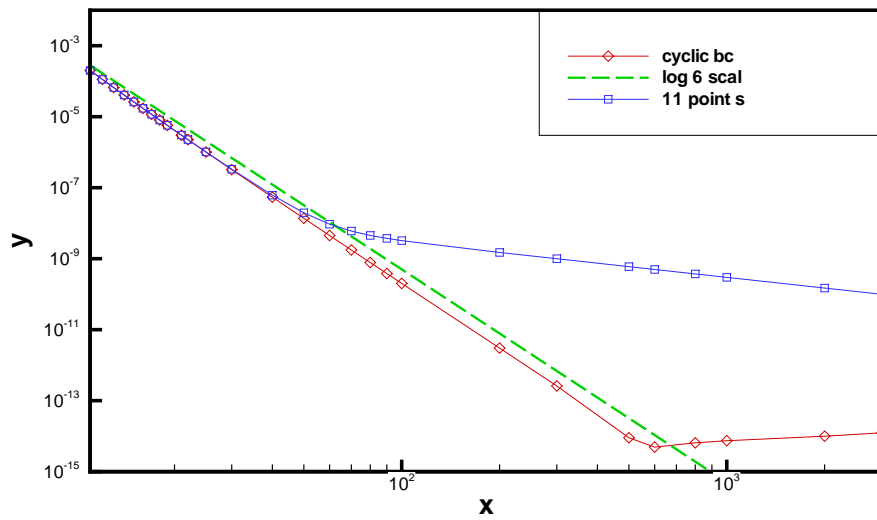
A two-dimensional version of the L_2 norm of eq. 8 is used to measure the numerical error, which is:

$$L_2 = \sqrt{\frac{\sum_{i=1}^N \sum_{j=1}^N (u_{i,j} - u_{exact})^2}{N^2}} \quad (12)$$

Figure 2 shows the comparison between the numerical and the analytical solution of the two-dimensional propagation of the acoustic pulse on the unbounded domain, at the computational time $\tilde{t} = 120$, using a uniform grid spacing equal to $\Delta\tilde{x} = \Delta\tilde{y} = 0.25$. There is no appreciable azimuthal distortion of the wave, showing that the numerical solution does not suffer from any appreciable degradation, and the isotropy is preserved in two dimensions. Figure 3 shows the L_2 norm at various levels of mesh refinement at $\tilde{t} = 120$. It is evident that sixth-order accuracy is maintained with a good approximation up to $L_2 \approx 1.0e - 9$.

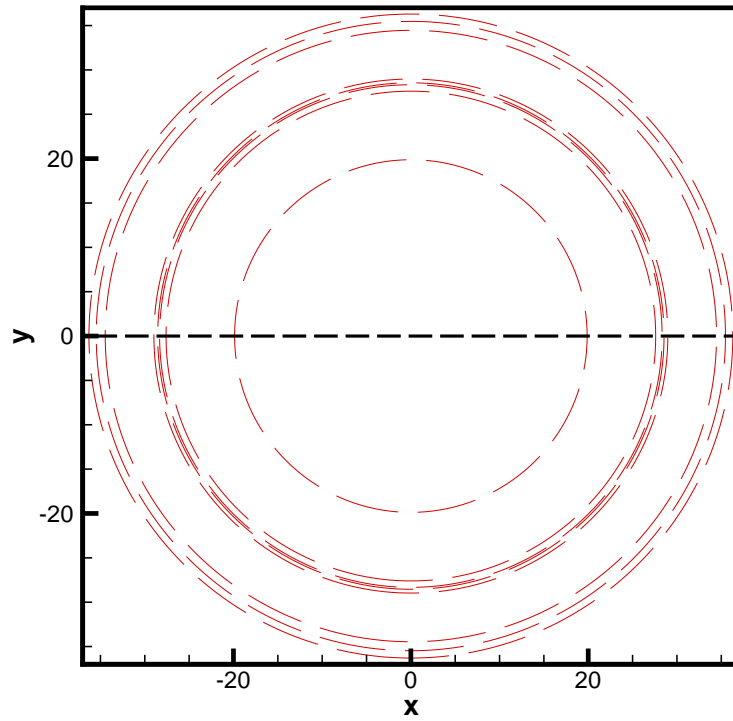


(a) Comparison between numerical and analytical solution with cyclic boundary conditions.

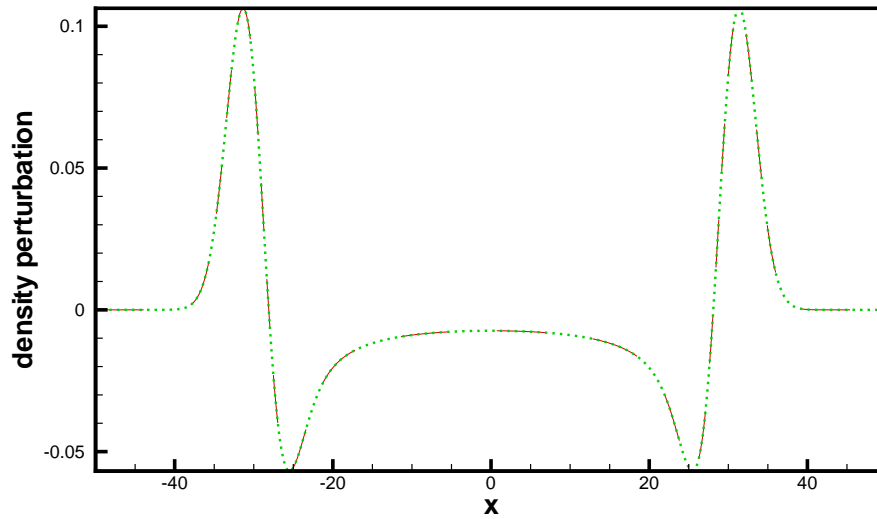


(b) L_2 norm error.

Figure 1. 1-D scalar advection equation with a sinusoidal monochromatic wave.



(a) Contours of non-dimensional density perturbation, contour levels: -0.02, 0.01, 0.02, 0.04.



(b) Non-dimensional density perturbation along the $y=0$ line.

Figure 2. Propagation of a two-dimensional acoustic pulse on an unbounded domain; dotted green line (\cdots) numerical prediction, long dash red line ($--$) analytical solution.

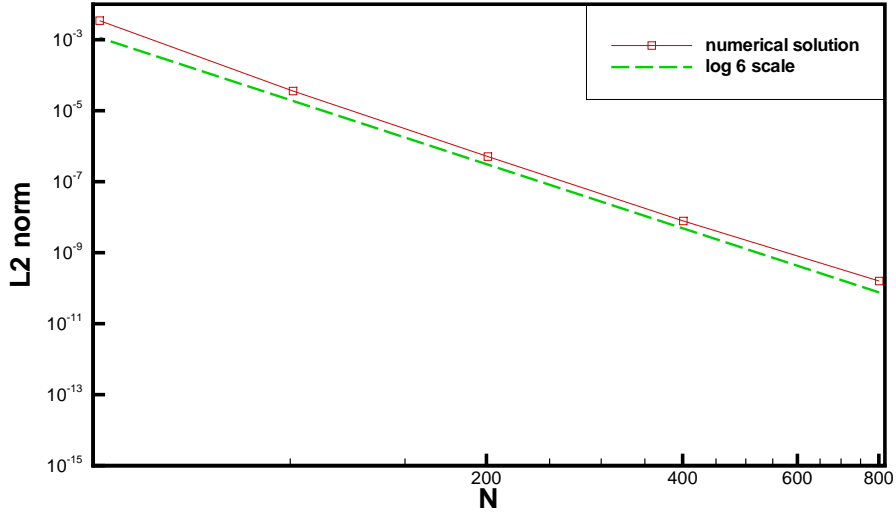


Figure 3. L_2 norm error for problem 2.

III. Inviscid wall boundary condition

A. Wall boundary condition and ghost value

1. Necessity of ghost values in finite difference equations

Consider the solid wall computational boundary at $y=0$ shown in figure 4. For points lying one row or more away from the wall ($m \geq 1$), the three-point stencil used for the interior computation lies entirely inside the physical domain. For the row of wall nodes ($m = 0$), the three-point stencil would extend outside the physical domain, so the interior scheme cannot be used here. It is necessary to introduce a boundary closure to simulate the presence of the wall, which requires a row of ghost nodes at $m = -1$ when a high-order scheme is used.

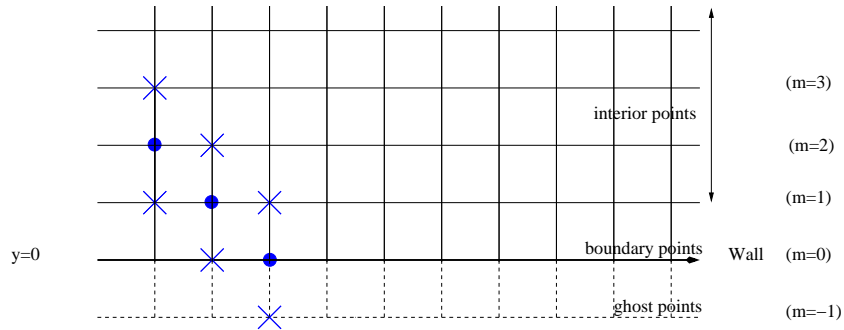


Figure 4. Near-wall boundary region.

Recall that the solution of the Euler or Navier-Stokes equations satisfies the PDEs at every interior or boundary point. In addition, at a point on the wall, the solution also satisfies the appropriate boundary condition. The governing equations of eq. 9, discretized in time and space, become a system of linear algebraic equations. In this system, each flow variable at either an interior or boundary point is governed by an algebraic equation, so the number of unknowns is exactly equal the number of equations. The boundary conditions at the wall has also to be satisfied, and must be added to the system of equations. However, in this way, there will be too many equations and not enough unknowns. This is one of the main differences between PDEs and algebraic equations. The extra conditions imposed on the flow variables by the wall

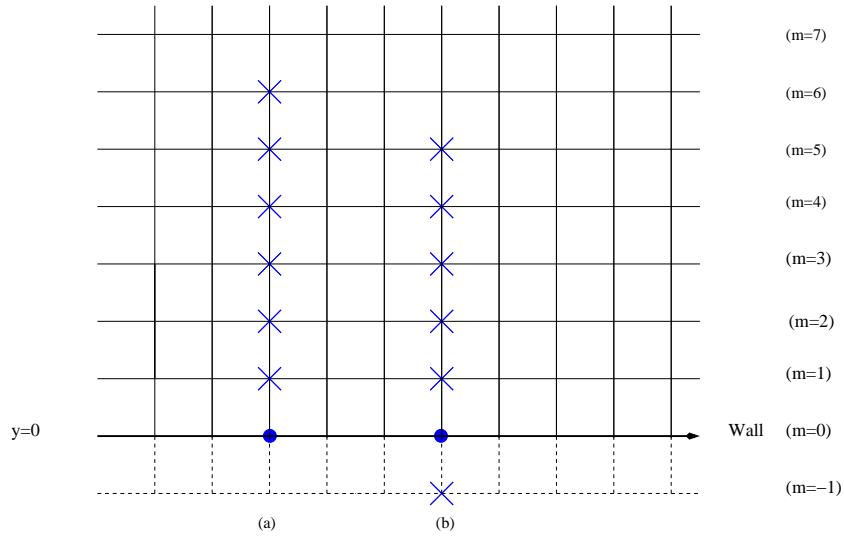


Figure 5. Seven-point stencil used to compute (a) the y -derivative of ρ , u and v , and (b) the y -derivative of p .

boundary conditions can be satisfied if ghost values are introduced (extra unknowns). These ghost points lie outside the computational domain and they have no physical meaning. For an inviscid wall, only one condition has to be imposed, that there is no mass flux through the wall. This requires a minimum of one ghost value per boundary point on the wall. From the physical point of view, the wall exerts a pressure on the fluid with a magnitude sufficient to make $v = 0$ at its surface. This can suggest the idea of using a fictitious value of pressure on the ghost node, just below the wall point, to simulate this pressure on the wall.

2. Asymmetric derivatives at boundary points

Consider the y -derivatives of the flow variables in the near-wall boundary region (fig 5). The wall boundary condition for the bottom wall is $v = 0$, at $y = 0$, where u, v are the velocity components in the x and y directions, respectively. The presence of one boundary condition implies the necessity of only one ghost node. The derivatives in the y direction for the flow variables ρ , u , and p , in the wall points is done using the one sided boundary stencil specified in section II-A. For the y -derivative of p , the stencil extends to the ghost point below the wall, and the formula for the forward derivative normal to the wall of the pressure at $m = 0$ is calculated using an asymmetric backward difference explicit stencil, accurate to the fourth order.⁵ Moreover, according to Hixon,¹⁶ the backward derivative normal to the wall of the pressure at the wall points is set to be equal and opposite to the forward derivative normal to the wall of the pressure at the wall points, to satisfy the condition of zero change of pressure at the wall in the normal direction ($\partial p / \partial y = 0$).

3. Setting the pressure at the ghost points

The ghost value of the pressure on the ghost point $(l-1)$, p_{l-1}^n , must be chosen so that the component of the velocity normal to the wall $v_{l,0}^n$ is zero at all times $n \Delta t$, for all n . This can be achieved by re-writing the y -momentum equation (third equation of eq. 9) at the wall points $(l, 0)$ using eq. 2:

$$v_{l,0}^{n+1} = v_{l,0}^n + h^{(4)} \quad (13)$$

with $h^{(4)}$ being the flux of v -velocity evaluated at the fourth Runge-Kutta stage (see eq. 3), and

$$F(\mathbf{U}^n) = -\frac{1}{\rho_0^n} \frac{\partial p_{l,0}^n}{\partial y} \quad (14)$$

or, in discretized form,:

$$F(\mathbf{U}^n) = -\frac{1}{\rho_0^n \Delta y} \sum_{j=1}^7 a_j^{51} p_{l,j-2}^n \quad (15)$$

where the coefficients a_j^{51} are given in Tam.⁵ Equations 13 and 15 are used to find $v_{i,0}^{n+1}$ after that all other physical quantities except $p_{i,-1}^n$ are found at the end of the n th time level. It is still necessary to impose the flow state at the wall to close the system (see section-III-A-4). To ensure that the wall boundary condition $v_{i,0}^{n+1} = 0$ is satisfied, the ghost value $p_{i,-1}^n$ can be found by setting $v_{i,0}^{n+1} = v_{i,0}^n = 0$ in eq. 13, for all n . By solving equation 15 for $p_{i,-1}^n$:

$$p_{i,-1}^n = -\frac{1}{a_{-1}^{51}} \sum_{j=2}^7 a_j^{51} p_{i,j-2}^n \quad (16)$$

Equation 16 is equivalent to setting the ghost value so that $\partial p / \partial y = 0$. It is important to stress that if no ghost value is introduced and the boundary condition $v_{i,0}^n = 0$ is imposed, the equation 13 will not, in general, be satisfied. This means that $\partial p / \partial y = 0$ will not necessarily equal zero at the wall.

4. Setting the flow state at the wall

Finally, to close the system, the flow state at the wall at the time $n\Delta t$ has to be imposed, after which all the physical quantities are defined in the interior region. To calculate the value of pressure, density and x -velocity at the wall, the non-penetration Neumann type condition is used. For the density, this condition becomes:

$$\frac{\partial \rho_{i,0}^n}{\partial y} = \frac{1}{\Delta y} \sum_{j=1}^7 s_j \rho_{i,j-1}^n = 0 \quad (17)$$

from which $\rho_{i,0}^n$ is equal to:

$$\rho_{i,0}^n = -\frac{1}{s_1} \sum_{j=2}^7 s_j \rho_{i,j-1}^n \quad (18)$$

with coefficients s_j given by Hixon,¹⁶ and similarly for $p_{i,0}^n$ and $u_{i,0}^n$.

To set the v -velocity on the wall, two different boundary closures are used. The first boundary closure is the classical non-penetration condition (called BC1):

$$v_{i,0}^n = 0 \quad (19)$$

The second one is the monotonicity-preserving boundary condition (called BC2). In a monotonicity preserving scheme, the sign of the gradient near the wall is unchanged in close proximity to the wall. This can be achieved by the use of a gradient limiter function.²⁴ An alternative approach is to constrain the rate of change of the gradient near the wall by imposing a suitable constraint on the near-wall curvature of the velocity. This approach fits particularly well simulations with acoustic reflections off a solid wall, where the wall-normal velocity gradient is finite and the wall-normal velocity and its curvature tend to zero for an infinite impedance (ideal) wall. Imposing $\frac{\partial^2 v_{i,0}^n}{\partial y^2} = 0$ at the wall enforces the monotonicity of the wall normal velocity gradient, strictly. In this paper, this condition is relaxed to

$$v_{i,0}^n + (\Delta y)^2 \frac{\partial^2 v_{i,0}^n}{\partial y^2} = 0 \quad (20)$$

Equation. 20 preserves the monotonicity of the wall-normal velocity in the presence of finite-amplitude pressure waves by constraining the change in the wall-normal velocity gradient to be of the order ($v/\Delta y < O(1)$), which is less than the near-wall gradient of the impinging acoustic wave of the order $O(k)$, where k is the wavenumber of the acoustic wave, due $v \rightarrow 0$ at the wall. This preserves the monotonicity of the wall-normal velocity in flows with a dominant wall-normal acoustic reflection, as proved by the standing wave equation being solution to equation. 20. An alternative interpretation of equation 20 is that a second-order $O(\Delta y^2)$ artificial viscosity term is added to the non-penetration boundary condition of equation 19. This second-order term damps the near-wall oscillations of v . The second-order derivative present in equation 20 is discretized using a second-order accurate upwind method:

$$\frac{\partial^2 v_{i,0}^n}{\partial y^2} = \frac{2v_{i,0}^n - 5v_{i,1}^n + 4v_{i,2}^n - v_{i,3}^n}{\Delta y^2} + O(\Delta y^2) \quad (21)$$

and so the value of $v_{i,0}^n$ is given by:

$$v_{i,0}^n = \frac{1}{3} (5v_{i,1}^n - 4v_{i,2}^n + v_{i,3}^n) \quad (22)$$

B. Numerical results

1. Two-dimensional acoustic wall reflection

To benchmark the two different boundary conditions BC1 and BC2, the reflection of an acoustic wave from a wall has been tested. This consists of the two-dimensional propagation of an acoustic wave in a fluid at rest ($u_0 = v_0 = 0$), against a bottom wall solid boundary. It is required to solve the LEE on uniform meshes with a computational domain of $-50 \leq \tilde{x} \leq 50$, $0 \leq \tilde{y} \leq 100$. At $\tilde{t} = 0$, the initial flow conditions are:

$$\begin{aligned}\tilde{p}' &= \tilde{\rho}' = e^{\left[-(\ln 2) \left(\frac{\tilde{x}^2 + (\tilde{y} - 25)^2}{25}\right)\right]} \\ \tilde{u}' &= \tilde{v}' = 0\end{aligned}\tag{23}$$

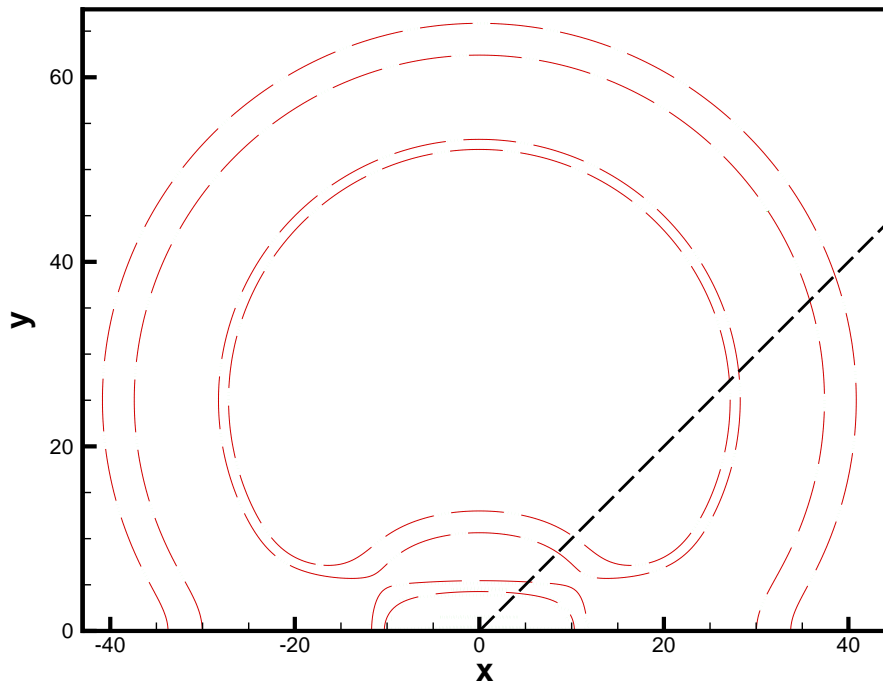
The computation is advanced in time up to the non-dimensional time $\tilde{t} = 120$, where the pulse has already impinged on the bottom wall, but not on the outflow computational boundaries, to check the accuracy properties of the wall boundary closure alone. The results are compared against the non-dimensional analytical perturbation values given in the first workshop on benchmark problems in Computational Aeroacoustics:²³

$$\tilde{p}' = \tilde{\rho}' = \frac{1}{2\alpha} \int_0^\infty e^{-\xi^2/4\alpha} \cos(\xi\tilde{t}) [J_0(\xi\eta) + J_0(\xi\zeta)] \xi d\xi\tag{24}$$

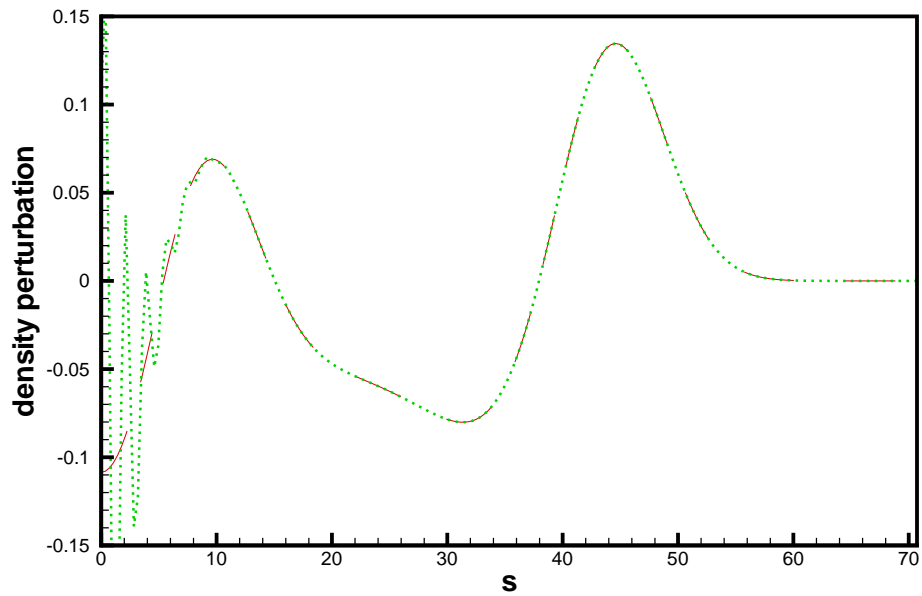
where $\alpha = [(\ln 2)/25]$, $\eta = \left[\left(\tilde{x}^2 + (\tilde{y} - 25)^2\right)\right]^{1/2}$, $\zeta = \left[\left(\tilde{x}^2 + (\tilde{y} + 25)^2\right)\right]^{1/2}$ and $J_0()$ is the zeroth-order Bessel function of the first kind. The same formulae for the numerical quadrature, tolerance error and L_2 norm of problem II-2 are used. Figures 6 and 7 show the contours of the calculated non-dimensional density perturbation at $\tilde{t} = 120$, using a uniform mesh spacing $\Delta\tilde{x} = \Delta\tilde{y} = 0.25$. The predictions are compared to the analytical reference solution. Figure 6 shows that with the first wall boundary closure (BC1), the numerical solution develops spurious high wavenumber oscillations near the wall. Figure 7 gives the numerical predictions using the monotonicity-preserving wall boundary condition (BC2). The new boundary condition prevents the formation of the spurious waves and the numerical solution follows to a good approximation the analytical one in the near-wall region. Figure 9 shows the L_2 norm using the same increasing levels of the mesh refinement as in problem II-2. The predictions are obtained using the same time step as for modelling the acoustic pulse in an unbounded domain of section II-2. The scheme is found to be numerically stable, therefore the monotonicity-preserving wall boundary BC2 preserves the global stability of the scheme. In figure 9 the L_2 norm decreases exponentially with increasing levels of mesh refinement. The logarithmic plot of fig. 9 shows the exponent being about 2.0, on the refined meshes. The global normalized error is driven by the wall boundary condition, which has been discretized using the second order spatial discretization of eq. 21. This has reduced the rate of convergence of the simulation to the third order on coarse meshes and to second order on refined meshes.

IV. Conclusion

This paper has presented an extension of the Tam and Dong solid wall boundary condition that combines the established non-penetration physical condition with a further restriction on the wall-normal velocity gradient. This results in a wall boundary condition in the form of a second-order partial differential equation which is satisfied analytically by fully reflecting acoustic waves and is monotonically preserving in problems with a dominant near-boundary acoustic pressure distribution. The wall boundary condition is implemented in a compact finite-difference time-marching scheme that is sixth-order accurate in space and fourth-order accurate in time. The order of accuracy of the interior scheme is verified by evaluating the mesh convergence rate in one and two dimensions for linear problems. With the extended wall boundary condition discretized to second-order spatial accuracy, tests on the wall reflection of a two-dimensional Gaussian pulse show that this condition suppresses the high wavenumber spurious numerical waves from the more conventional $v = 0$ formulation. This result is obtained without the use of high-order filters applied to the computational domain interior. The mesh convergence study on the extended boundary condition test case shows that the scheme L_2 norm reduces as for a second-order scheme. Whilst this reduces the efficiency of the numerical method for CAA applications, the second order convergence derives from the discretization of the boundary condition rather than from its underlying differential form. Tests with higher order finite-difference approximations

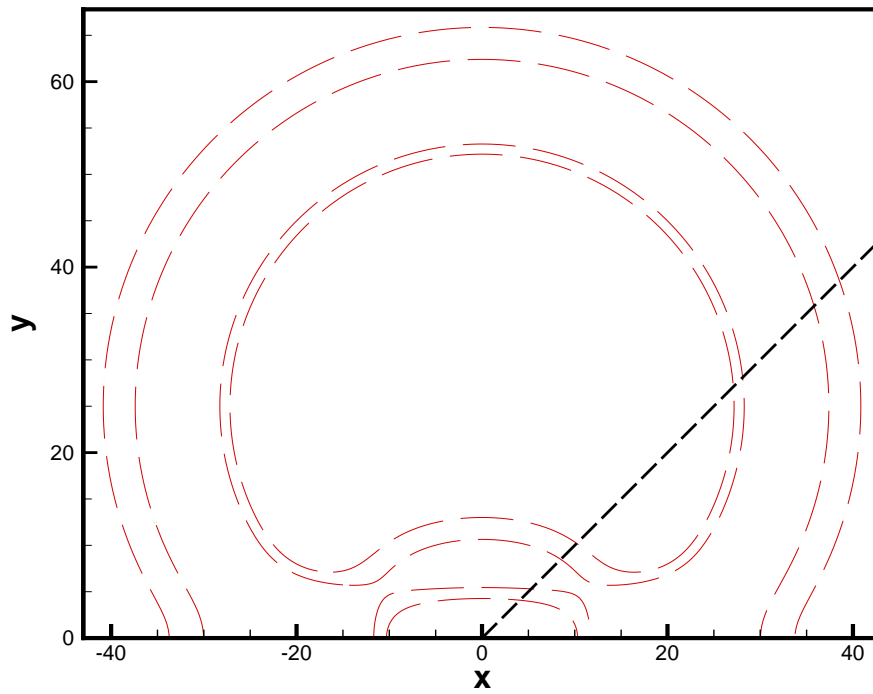


(a) Contours of non-dimensional density perturbation, contour levels: 0.01, 0.05.

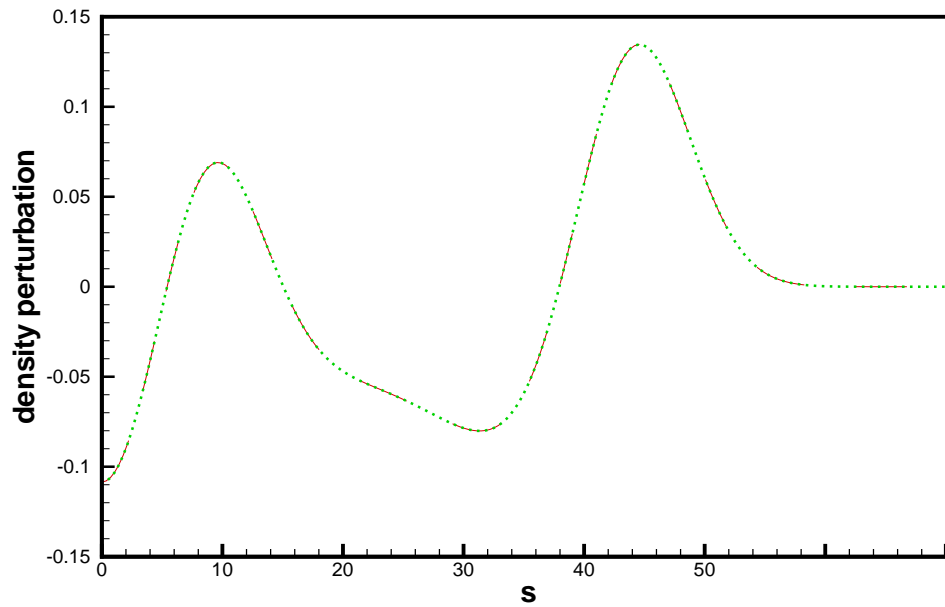


(b) Non-dimensional density perturbation along the $y=x$ line.

Figure 6. BC1: Wall reflection of a two-dimensional acoustic pulse; dotted green line (\cdots) numerical prediction, long dash red line ($---$) analytical solution.



(a) Contours of non-dimensional density perturbation, contour levels: 0.01, 0.05.



(b) Non-dimensional density perturbation along the $y=x$ line.

Figure 7. BC2: Wall reflection of a two-dimensional acoustic pulse; dotted green line (\cdots) numerical prediction, long dash red line ($--$) analytical solution.

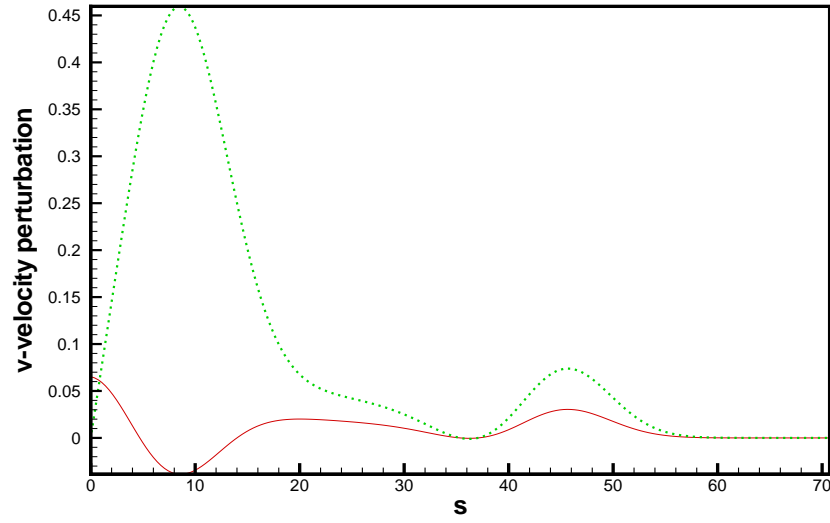


Figure 8. BC2: Non-dimensional v -velocity perturbation along the $y=x$ line

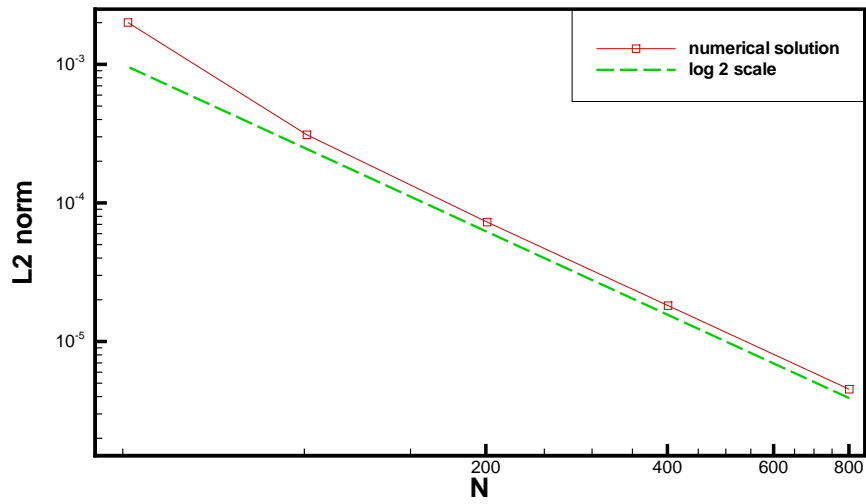


Figure 9. L_2 norm error for problem **B**.

for the monotonicity-preserving wall boundary condition are in progress towards preserving the order of accuracy of the interior scheme.

Acknowledgements

This research project has been supported by a Marie Curie Early Stage Research Training Fellowship of the European Community's Sixth Framework Programme under contract number MEST CT 2005 020301.

References

- ¹Colonius, T. and Lele, S., "Computational aeroacoustics: progress on nonlinear problems of sound generation," *Progress in Aerospace Sciences*, Vol. 40, 2004, pp. 365–416.
- ²Colonius, T., "Modeling artificial boundary conditions for compressible flow," *Annual Review of Fluid Mechanics*, Vol. 40, 2004, pp. 315–345.
- ³Tam, C. K. W., "Computational Aeroacoustics: Issues and Methods," *AIAA paper*, 1995, 95-0677.
- ⁴Lele, S. K., "Compact finite difference schemes with spectral-like resolution," *Journal of Computational Physics*, Vol. 103, No. 1, 1992, pp. 16–42.
- ⁵Tam, C. K. W. and Dong, Z., "Wall boundary conditions for high-order finite-difference schemes in computational aeroacoustics," *Theoretical and Computational Fluid Dynamics*, Vol. 6, 1993, pp. 303–322.
- ⁶Colonius, T., Lele, S. K., and Moin, P., "Boundary Conditions for Direct Computation of Aerodynamic Sound Generation," *AIAA Journal*, Vol. 31, No. 9, September 1993.
- ⁷Tam, C. K. W., Web, J. C., and Dong, Z., "A study of short wave components in computational acoustics," *J. Comput. Acoustics*, Vol. 1, 1993, pp. 1–30.
- ⁸Vichnevetsky, R., "Wave propagation analysis of difference schemes for hyperbolic equations. A review," *International Journal for Numerical Methods in Fluids*, Vol. 7, No. 5, 1987, pp. 409–452.
- ⁹Kurbatskii, K. A. and Mankbadi, R. R., "Review of computational aeroacoustics algorithms," *International Journal of Computational Fluid Dynamics*, Vol. 18, No. 6, 2004, pp. 533–546.
- ¹⁰Jameson, A., Schmidt, W., and Turkel, E., "Numerical solution of the Euler equations by finite volume methods using Runge-Kutta time-stepping schemes," *AIAA paper*, Vol. 81, June 1981.
- ¹¹Tam, C. K. W. and Web, J. C., "Dispersion-Relation-Preserving finite difference schemes for Computational Acoustics," *Journal of Computational Physics*, Vol. 107, 1993, pp. 262–281.
- ¹²Lockard, D. P., Brentner, K. S., and Atkins, H. L., "High-accuracy algorithms for computational aeroacoustics," *AIAA Journal*, Vol. 33, No. 2, 1995, pp. 246–251.
- ¹³Visbal, M. R. and Gaitonde, D. V., "Computation of aeroacoustic fields on general geometries using compact differencing and filtering schemes," *30th AIAA Fluid Dynamic Conference*, No. 3706, American Institute of Aeronautics and Astronautics, June 1999.
- ¹⁴Hixon, R., "Prefactored compact filters for computational aeroacoustics," Conference paper 1999-358, *37th Aerospace Sciences Meeting and Exhibit*, Reno, NV, Jan. 1999.
- ¹⁵Rona, A. and Spisso, I., "A selective overview of high-order finite difference schemes for aeroacoustic applications," *14th International Conference on Sound and Vibration*, Cairns, Australia, 2007.
- ¹⁶Hixon, R., "Prefactored small-stencil compact schemes," *Journal of Computational Physics*, Vol. 165, No. 2, 2000, pp. 522–41.
- ¹⁷Carpenter, M. H., Gottlieb, D., and Aberbanel, S., "Stable and accurate boundary treatments for compact, high-order finite-difference schemes," *Applied Numerical Mathematics*, Vol. 12, 1993, pp. 55–87.
- ¹⁸Carpenter, M. H., Gottlieb, D., and Aberbanel, S., "Time-stable boundary conditions for finite-difference schemes solving hyperbolic systems: methodology and application to high-order compact schemes," *Journal of Computational Physics*, Vol. 111, 1994, pp. 220–236.
- ¹⁹Kim, J. W. and Lee, D. J., "Implementation of boundary conditions for optimized high-order compact schemes," *J. Comput. Acoustics*, Vol. 5, No. 2, June 1997, pp. 177–191.
- ²⁰Hixon, R., "A New Class of Compact Schemes," Conference paper 1998-367, *37th Aerospace Sciences Meeting and Exhibit*, Reno, NV, January 1998.
- ²¹Hirsch, C., *Numerical Computation of Internal and External flow*, New York, 1988.
- ²²Hixon, R., "On Increasing the accuracy of MacCormack schemes for Aeroacoustic Applications," Nasa Contract Report 202311 ICOMP-96-11, NASA, December 1996.
- ²³Hardin, J., Ristorcelli, J. R., and Tam, C., editors, *ICASE/LaRC Workshop on Benchmark Problems in Computational Aeroacoustics (CAA)*, Hampton, Virginia, October 1995, NASA Conference Publication 3300.
- ²⁴Sweby, P., "High resolution schemes using flux limiters for hyperbolic conservative laws," *SIAM Journal of Numerical Analysis*, Vol. 21, No. 5, October 1984, pp. 995–1011.